



# Effects of oxidation on structure and performance of $\text{LiVPO}_4\text{F}$ as cathode material for lithium-ion batteries

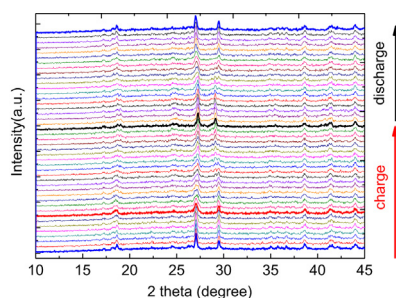
Rui Ma, Lianyi Shao, Kaiqiang Wu, Miao Shui, Dongjie Wang, Nengbing Long, Yuanlong Ren, Jie Shu\*

Faculty of Materials Science and Chemical Engineering, Ningbo University, Ningbo 315211, Zhejiang Province, People's Republic of China

## HIGHLIGHTS

- $\text{LiVPO}_4\text{F}$  transforms into  $\text{Li}_{1-x}\text{VPO}_4\text{F}_{1-y}\text{O}_z$  after oxidation in air.
- A transformation of  $\text{LiVPO}_4\text{F} \rightarrow \text{Li}_{0.72}\text{VPO}_4\text{F} \rightarrow \text{VPO}_4\text{F}$  appears for  $\text{LiVPO}_4\text{F}$  during charge.
- $\text{Li}_{1-x}\text{VPO}_4\text{F}_{1-y}\text{O}_z$  shows stable structure upon delithiation.

## GRAPHICAL ABSTRACT



## ARTICLE INFO

### Article history:

Received 13 August 2013

Received in revised form

21 September 2013

Accepted 9 October 2013

Available online 17 October 2013

### Keywords:

Fluorophosphate

Oxidation

Cathode material

Lithium-ion batteries

*In-situ* X-ray diffraction

## ABSTRACT

In this paper, a series of  $\text{LiVPO}_4\text{F}$ -based samples are prepared through sintering  $\text{LiVPO}_4\text{F}$  at different temperatures under air. Experimental results show that the pristine sample is oxidized to a new compound  $\text{Li}_{1-x}\text{VPO}_4\text{F}_{1-y}\text{O}_z$  ( $0 < x < 0.2$ ,  $0.9 < y \leq 1$ ,  $0.9 < z \leq 1$ ) with similar structure of  $\text{LiVPO}_4\text{O}$  under air at  $550^\circ\text{C}$  or higher one. *In-situ* X-ray diffraction patterns indicate that the original material  $\text{LiVPO}_4\text{F}$  undergoes two two-phase structural evolutions upon  $\text{Li}^+$  electrochemical extraction at average operating potentials at 4.26 and 4.30 V, corresponding to the continuous transformation of  $\text{LiVPO}_4\text{F} \rightarrow \text{Li}_{0.72}\text{VPO}_4\text{F} \rightarrow \text{VPO}_4\text{F}$  in the first charge process. In the reverse discharge process, there is only one two-phase structural transition  $\text{VPO}_4\text{F} \rightarrow \text{LiVPO}_4\text{F}$  without the appearance of the intermediate phase  $\text{Li}_{0.72}\text{VPO}_4\text{F}$  on  $\text{Li}^+$  insertion reaction at 4.18 V. Therefore, the extraction/insertion process of  $\text{LiVPO}_4\text{F}$  is an asymmetrical phase transformation. When the sintering temperature is raised to  $550^\circ\text{C}$ ,  $\text{Li}_{1-x}\text{VPO}_4\text{F}_{1-y}\text{O}_z$  exhibits extremely poor electrochemical performance, which is attributed to the volatilization loss of lithium and the replacement of fluorine by oxygen in the structure during the sintering process under air. However,  $\text{Li}_{1-x}\text{VPO}_4\text{F}_{1-y}\text{O}_z$  has a very stable structure during the whole process of galvanostatic charge/discharge cycles as confirmed by *in-situ* X-ray diffraction technique.

© 2013 Elsevier B.V. All rights reserved.

## 1. Introduction

In the past ten years, lithium-ion batteries have been extensively applied to various portable electronic products, such as laptops, cell

phones and digital cameras, resulted from miniaturization technologies. Nowadays, the application of lithium-ion batteries in large-scale devices such as power electric and hybrid electric vehicles, energy-efficient cargo ship, locomotives and aerospace are being driven by an ever-increasing demand, seriously environmental issues and ever-increasing cost of fossil fuels. However, there are many key factors in electrode materials, such as working potential, energy density, power capability, cycle lifetime, stable

\* Corresponding author. Tel.: +86 574 87600787; fax: +86 574 87609987.

E-mail addresses: [sergio\\_shu@hotmail.com](mailto:sergio_shu@hotmail.com), [shujie@nbu.edu.cn](mailto:shujie@nbu.edu.cn) (J. Shu).

structure and security problems, need to be improved before lithium-ion batteries could be applied to large-scale devices [1–6]. Owing to the pivotal role of cathode materials in high power lithium-ion batteries, much attention is paid to the development of cathode materials such as layer-structured  $\text{LiMO}_2$  ( $M = \text{Co}, \text{Ni}, \text{Mn}$ ) [7,8], spinel-structured  $\text{LiMn}_2\text{O}_4$  [9,10], olivine-structured  $\text{LiMPO}_4$  ( $M = \text{Fe}, \text{Mn}, \text{Co}$ ) [11–15], vanadium oxide ( $\text{V}_2\text{O}_5$ ,  $\text{LiV}_3\text{O}_8$ ) [16–18], Nasicon-type  $\text{Li}_x\text{M}_2(\text{PO}_4)_3$  ( $M = \text{Fe}, \text{V}, \text{Ti}$ ) [19], fluorine-containing transition metal phosphates and sulfates  $\text{A}_x\text{M}(\text{XO}_4)\text{F}$  ( $A = \text{Li}; M = \text{V}, \text{Fe}, \text{Ti}; X = \text{P}, \text{S}$ ) [20–24].

Inspired pioneering work by Barker [25,26],  $\text{LiVPO}_4\text{F}$ , as an attractive cathode material for the next generation of lithium-ion batteries, is a novel fluorophosphate material based on the phosphate polyanion. In the crystal structure, the strong inductive effect of the  $\text{PO}_4^{3-}$  polyanion moderates the energetics of the transition-metal redox couple to generate the relatively high operating potentials. Additionally, the effect of the presence of additional fluorine atom on this inductive effect in the structure of  $\text{LiVPO}_4\text{F}$  is beneficial to develop novel polyanion systems in the future, i.e. the V–F bond is very stable, which results in the structure of  $\text{LiVPO}_4\text{F}$  remaining stable upon repeated  $\text{Li}^+$  extraction/insertion reactions [26]. However,  $\text{LiVPO}_4\text{F}$  exposed to air/moisture is difficult to avoid the surface oxidation and moisture-absorption, which will result in the structural changes of  $\text{LiVPO}_4\text{F}$ . As a result, it may show poor electrochemical performance due to partial vanadium oxidation and/or lithium and fluorine loss similar with those appeared on oxidized  $\text{LiFePO}_4$  [27].

Therefore, this work is to investigate the effects of oxidation on the structure and performance of  $\text{LiVPO}_4\text{F}$  as cathode materials for lithium-ion batteries through a combination of several powerful techniques such as thermogravimetry and differential thermal analysis (TG–DTA), thermogravimetry, differential scanning calorimetry and mass spectrometry (TG–DSC–MS), inductively coupled plasma atomic emission spectrometer (ICP–AES), energy dispersive spectrometer (EDS), X-ray fluorescence spectrometer (XRF), X-ray photoelectron spectrometer (XPS), Fourier transform infrared spectrometer (FTIR), powder and *in-situ* X-ray diffraction (XRD) techniques. It is found that the pristine  $\text{LiVPO}_4\text{F}$  shows an asymmetrical structural evolution but oxidized  $\text{LiVPO}_4\text{F}$  with similar structure of  $\text{LiVPO}_4\text{O}$  shows almost no structural transformation during charge/discharge process.

## 2. Experimental

### 2.1. Synthesis of $\text{LiVPO}_4\text{F}$ -based samples

The synthesis of pristine  $\text{LiVPO}_4\text{F}$  was similar with the method reported by Barker [9]. Firstly,  $\text{V}_2\text{O}_5$  (AR,  $\geq 99.0\%$ ),  $\text{NH}_4\text{H}_2\text{PO}_4$  (AR,  $\geq 99.0\%$ ) and acetylene black (25% mass excess) with a stoichiometric amount were mixed and sintered to yield the intermediate phase  $\text{VPO}_4$ , and then  $\text{LiF}$  was added to obtain the original material  $\text{LiVPO}_4\text{F}$ . Detailed synthetic steps of  $\text{LiVPO}_4\text{F}$  were reported in our previous paper [28]. Afterward, a series of  $\text{LiVPO}_4\text{F}$ -based samples were prepared through sintering  $\text{LiVPO}_4\text{F}$  over a temperature range between 350 and 750 °C for 30 min under air.

### 2.2. Electrode and cell preparation

The working electrode was prepared by mixing 80%  $\text{LiVPO}_4\text{F}$ -based samples and 10% polyvinylidene fluoride and 10% carbon black. This powder mixture was manually ground and then dissolved in N-methylpyrrolidone to form homogeneous slurry, and then the slurry was coated on Al foil, dried at 120 °C for 12 h in a vacuum oven, and cut into discs with a diameter of 15 mm. For cell fabrication, the counter electrode is Li metal disc, the separator is

Whatman glass fiber diaphragm, and the electrolyte is comprised of 1 mol  $\text{L}^{-1}$   $\text{LiPF}_6$  in ethylene carbonate and dimethyl carbonate with a volume ratio of 1:1.

### 2.3. Analytical methods

The thermogravimetry and differential thermal analysis behaviors of  $\text{LiVPO}_4\text{F}$  were investigated on a Seiko TG/DTA 6300 instrument under air over a temperature range between 20 and 800 °C with a heating rate of 5 °C  $\text{min}^{-1}$ . The cooling process was conducted under natural conditions. Thermogravimetry, differential scanning calorimetry and mass spectrometry tests were performed by a NETSCH STA 449C combined with a NETSCH 403C Aeolos II quadrupole mass spectrometer. The test temperature range was from 30 to 550 °C with a heating rate of 10 °C  $\text{min}^{-1}$  under argon with an oxygen flowing rate of 18 ml  $\text{min}^{-1}$ . Simultaneously, the gaseous products formed in thermal reaction were monitored by the connected mass spectrometer. Powder X-ray diffraction patterns were collected on a Bruker D8 Focus diffractometer (40 kV, 40 mA), using  $\text{Cu-K}\alpha$  radiation. The scanning angle  $2\theta$  was in a range from 10 to 80° with a scanning rate of 4°  $\text{min}^{-1}$ . The surface morphologies and element compositions of  $\text{LiVPO}_4\text{F}$ -based samples were characterized by Hitachi S3400 scanning electron microscopy (SEM) and Oxford INCA energy dispersive spectrometer. Inductively coupled plasma atomic emission spectrometer (Perkin Elmer Optima 2100 DV) was employed to determine the mole ratio (At.%) of Li, P and V in the original  $\text{LiVPO}_4\text{F}$  and the oxidized samples. The valence states of vanadium in the original  $\text{LiVPO}_4\text{F}$  and the samples sintered at 550 °C for 30 min under air were determined by X-ray photoelectron spectrometer (Kratos Model XSAM800) equipped with an Mg  $\text{K}\alpha$  achromatic X-ray source ( $h\nu = 1235.6$  eV). X-ray fluorescence spectrometer (Bruker S2 Ranger) was employed to determine the mole ratio (At.%) of P and V in the original  $\text{LiVPO}_4\text{F}$  and the samples sintered at 550 °C for 30 min under air. Fourier transform infrared spectroscopy measurements were carried out on Shimadzu FTIR-8900 spectrometer with a distinguishability of 4  $\text{cm}^{-1}$  between 400 and 4000  $\text{cm}^{-1}$ .  $\text{LiVPO}_4\text{F}$ -based samples were manually ground with KBr and then pressed into thin slices for FTIR analysis.

The galvanostatic charge/discharge tests were performed on LAND CT2001A battery test system (Wuhan Jinnuo, China). Lithium-ion batteries were cycled between 3.0 and 4.7 V at a current density of 10 mA  $\text{g}^{-1}$ . Cyclic voltammetry (CV) tests were performed between 3.0 and 4.7 V with a scanning rate of 0.1 mV  $\text{s}^{-1}$  on CHI 660D electrochemical workstation (Shanghai Chenhua, China) at room temperature.

The *in-situ* structural evolutions of  $\text{LiVPO}_4\text{F}$  and the oxidized sample obtained at 550 °C during  $\text{Li}^+$  extraction/insertion were observed by *in-situ* X-ray diffraction using the same Bruker D8 Focus diffractometer as described above. Prior to the *in-situ* X-ray diffraction tests,  $\text{LiVPO}_4\text{F}$  powders and the oxidized sample were respectively mixed with carbon black and subsequently ground in agate mortar and then ready for the following *in-situ* X-ray diffraction tests. All simulated cells and *in-situ* cells were assembled in an argon-filled glovebox with relative humidity under 5 ppm.

The homemade *in-situ* cell used in this work is designed based on the adjustment of *in-situ* Raman cell reported by our previous paper [29,30]. It mainly consists of stainless steel chamber, beryllium disc, working electrode, separator, lithium disc, stainless steel disc and polytetrafluoroethylene sleeve. Dozens of milligrams powders mixed with carbon black were prepared in advance as the working electrode by directly putting on the beryllium window of the *in-situ* cell, and then separator, lithium metal, stainless steel disc and electrolyte are placed in turn in the *in-situ* cell chamber. All the collected *in-situ* X-ray diffraction data were analyzed using the Fullprof program.

### 3. Results and discussion

Fig. 1 presents the TG–DTA curves of the original material  $\text{LiVPO}_4\text{F}$  between ambient temperature and 800 °C under air. Two weight losses could be observed in the TG curve with a total weight loss of 7.84%. The first weight loss (0.7%) between 100 and 150 °C is associated with the dehydration process resulted from physically absorbed water [31]. The major weight loss (7.14%) is observed from 400 to 550 °C in the TG curve, which is probably attributed to the removal of residual carbon (approximate 5.21%), the partial volatilization loss of lithium (approximate 0.40%) and the replacement of fluorine by oxygen (approximate 1.53%) under air [27,29], corresponding to the strong exothermic peak in the DTA curve appearing at approximate 470 °C. The element loss is also confirmed by the TG–DSC–MS, ICP–AES, EDS, XRF and XPS results of oxidized  $\text{LiVPO}_4\text{F}$  at 550 °C as shown in Table 1.

Fig. 2 shows the TG–DSC–MS results of the original material  $\text{LiVPO}_4\text{F}$  under oxygen. Similar with the results of TG–DTA, it could also be found that the original sample shows obvious weight loss and exothermic peak at a temperature range from 350 to 550 °C. Four channels of MS signals with high resolution of ion current ( $10^{-11} \text{ A}^{-1}$ ) were monitored each time synchronously. Here, the channels of  $m/z = 20$ , 26, 30 and 38 were recorded in the experiment. It is found that the signal of  $m/z = 26$  was observed, which is probable contributed to volatilization loss of LiF at high temperature solid reaction calcination. However, no signal of  $m/z = 20$ , 30 and 38 could be found in the experiment. Therefore, the thermal decomposition products of  $\text{LiVPO}_4\text{F}$  under oxygen cannot be assigned to  $\text{H}_2\text{O}$ , HF,  $\text{Li}_2\text{O}$  and  $\text{F}_2$ .

In this paper, a series of  $\text{LiVPO}_4\text{F}$ -based powders were prepared under air by sintering  $\text{LiVPO}_4\text{F}$  at 350, 550, 600, 650, 700 and 750 °C for 30 min. For investigating the effects of oxidation degree on the morphology and structure of  $\text{LiVPO}_4\text{F}$ , powder XRD patterns and corresponding SEM images are collected in the experiment. Figs. 3 and 4 show the XRD patterns of  $\text{LiVPO}_4\text{F}$ -based samples heat-treated at different temperatures. The main diffractions peaks of  $\text{LiVPO}_4\text{F}$  located at  $18.1^\circ$ ,  $18.6^\circ$ ,  $22.4^\circ$ ,  $26.2^\circ$ ,  $27.1^\circ$ ,  $29.5^\circ$  are in accordance with the crystal faces (010), (100), (110), ( $-111$ ), (0–11) and (1–10), respectively, corresponding to the JCPDS card No.22–1138 and previous reports [25,26,32]. The detailed structural parameters of  $\text{LiVPO}_4\text{F}$  are described in Table S1 (Supplementary materials). When  $\text{LiVPO}_4\text{F}$  powder was sintered at 350 °C for 30 min under air, it could be found that there was no significant difference in the crystal structure with that of the pristine sample [26,32], but the SEM image presents a few agglomeration phenomena as shown in Fig. 5. When the sintering temperature was raised to 550 °C, the powder particles appears to be non-uniform

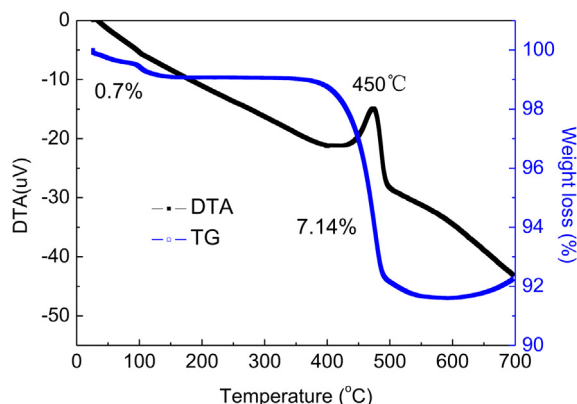


Fig. 1. DTA–TG curves of the original material  $\text{LiVPO}_4\text{F}$  under air.

Table 1

The final chemical composition of  $\text{LiVPO}_4\text{F}$ -based materials.

Sample	ICP-AES	EDS	XRF	XPS	The possible final chemical composition
	Mole ratio (At.%)				
	Li:P:V	P:V:F	P:V	Li:P:F	
The original	0.98:1:0.93	1:0.92:1.24	1:1.12	1:0.64:0.38	LiVPO <sub>4</sub> F
LiVPO <sub>4</sub> F-350 °C	1.05:1:1.07	1:0.91:1.09	/	/	LiVPO <sub>4</sub> F
LiVPO <sub>4</sub> F-550 °C	0.92:1:1	1:0.97:0	1:1.16	1:0.64:0.04	Li <sub>1-x</sub> VPO <sub>4</sub> F <sub>1-y</sub> O <sub>z</sub>
LiVPO <sub>4</sub> F-600 °C	0.85:1:0.95	1:0.97:0	/	/	Li <sub>1-x</sub> VPO <sub>4</sub> O
LiVPO <sub>4</sub> F-650 °C	0.83:1:0.92	1:1:0	/	/	Li <sub>1-x</sub> VPO <sub>4</sub> O
LiVPO <sub>4</sub> F-700 °C	/	1:0.87:0	/	/	/

Here,  $0 < x < 0.2$ ,  $0.9 < y \leq 1$ ,  $0.9 < z \leq 1$ .

and somewhat larger as seen in Fig. 5. Although the whole shape of XRD pattern is maintained after sintering, all the diffraction peaks of the oxidized samples shift to higher Bragg positions and become sharper as shown in Fig. 4. As reported, the thermal decomposition of  $\text{LiFePO}_4$  at a sintering temperature higher than 500 °C resulted in the formation of  $\text{Fe}_2\text{O}_3$  and oxidized  $\text{Li}_x\text{Fe}_y\text{PO}_4$  under air [27]. However, no featured diffraction peak of  $\text{V}_2\text{O}_5$ ,  $\text{Li}_3\text{PO}_4$  or  $\text{Li}_3\text{V}_2(\text{PO}_4)_3$  can be found in the XRD patterns. Although both  $\text{LiVPO}_4\text{F}$  and  $\text{LiFePO}_4$  are based on the phosphate polyanion cathode materials, the structural evolutions of  $\text{LiVPO}_4\text{F}$  under air are different with those of  $\text{LiFePO}_4$ . As reported [33–35], anion- or cation-deficient/doped behavior in multi-element compounds always induces the shift of diffraction peaks in the XRD patterns. Here, all the samples were heat-treated under air in the experiment. Therefore, the fluorine atoms can be replaced by the oxygen atoms in the structure during high temperature calcination. With a careful XRD investigation, it is found that these diffraction peaks are similar with the formation of  $\text{LiVPO}_4\text{O}$  compound (space group: P-1) based on the JCPDS card No.72–2253. Therefore, the oxidized compounds are probable the derivatives of  $\text{LiVPO}_4\text{O}$  and isostructural with the known mineral ambygonite,  $\text{LiVPO}_4\text{O}$ .

To describe the proper composition of  $\text{LiVPO}_4\text{F}$ -based samples, the molar ratios of various elements in the compounds were tested and analyzed through the combination of ICP–AES, SEM–EDS, XPS

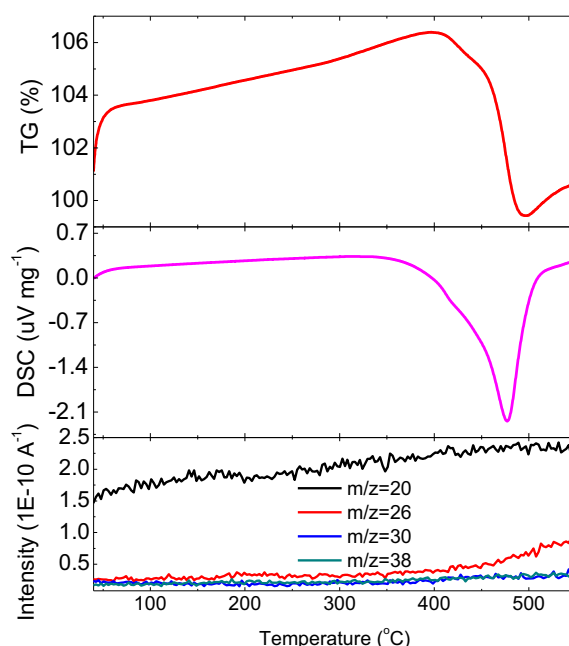


Fig. 2. TG–DSC–MS results of the original material  $\text{LiVPO}_4\text{F}$  under oxygen.

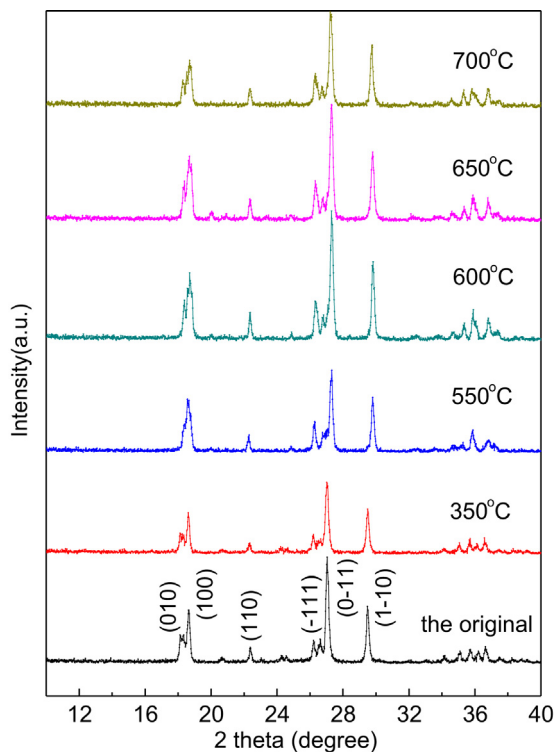


Fig. 3. XRD patterns of LiVPO<sub>4</sub>F-based samples heat-treated at different temperatures.

and XRF methods. The analytical results of various techniques are summarized in Table 1 and the patterns of SEM-EDS could be seen in Fig. 6. Except for the existence of Li, V, P and O elements, it is found that almost no F element can be observed by ICP-AES, SEM-EDS and XRF. For comparison, trace F element can be detected by XPS as shown in Fig. 7.

The core level XPS spectra of the original LiVPO<sub>4</sub>F and the sample sintered at 550 °C for 30 min under air are shown in Fig. 7a. All the obtained binding energy (BE) values are calibrated by the C 1s standard spectrum (284.80 eV) as shown in Fig. 7b. The binding energy values of V 2p are 517.38 and 524.81 eV, corresponding to energy level of V 2p<sub>3/2</sub> and V 2p<sub>1/2</sub>, respectively, as shown in Fig. 7c. The energy difference between V 2p<sub>3/2</sub> and V 2p<sub>1/2</sub> is due to the spin orbit coupling [36]. The BE value of V 2p<sub>3/2</sub> of the original LiVPO<sub>4</sub>F matches well with the values observed in LiVPO<sub>4</sub>F (517.20 eV) [37,38], indicating that the oxidation state of vanadium of the original LiVPO<sub>4</sub>F is 3+. It means that the V<sup>5+</sup> has been reduced to V<sup>3+</sup> during the carbothermal reduction process. However, the main oxidation state of vanadium in the sample sintered at 550 °C for 30 min under air is +4 with the V 2p BE values of 518.09 and 525.38 eV, which suggests that the original LiVPO<sub>4</sub>F transforms into a new compound with isostructure of LiVPO<sub>4</sub>O. The spectrum of O 1s for the original sample is also shown in Fig. 7d, and the BE value of 531.83 eV is characteristic of O element in the O–V or O–P bond [36], which is similar to the BE value of O 1s in LiFePO<sub>4</sub> (531.60 eV) [39]. The spectrum of F 1s for the original sample is shown in Fig. 7e, and the BE value of 685.77 eV is the characteristic of the V–F bond [36], which is similar to the BE value of F 1s in Li–F bond (685.70 eV). The spectrum of P 2p for the original sample is shown in Fig. 7f, and the BE value of 134.03 eV is the characteristic of the P in PO<sub>4</sub> tetrahedra, which is similar to the BE value of P 2p in LiFePO<sub>4</sub> (133.50 eV) [39]. Compared the O, F, P spectra before and after oxidation, it is clear that the BE values for O, F and P do not change after sintered at 550 °C for 30 min under air, which suggests that the chemical valence states for O (–2), F (–1) and P (+5) maintain

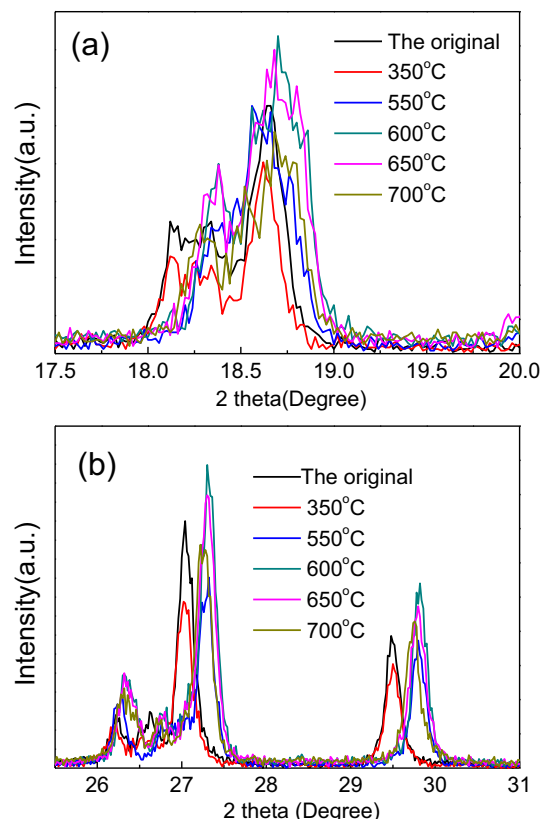
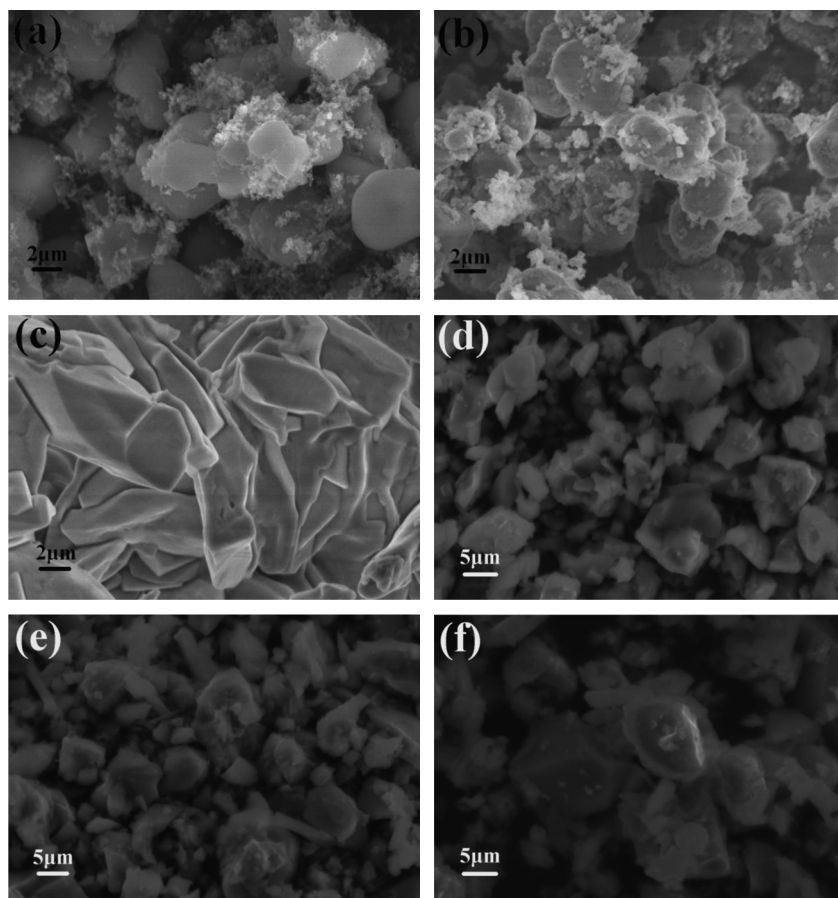


Fig. 4. Selected XRD patterns of LiVPO<sub>4</sub>F-based samples heat-treated at different temperatures. (a) 17.5–20.0°; (b) 25.5–31.0°.

the original values in the compound before and after oxidation. Based on the above analysis, it can be found that there is a small number of F still existing in the oxidized sample after sintering under air. For comparison, the content of Li in the oxidized sample just shows few decreases. Therefore, we concluded that the original material LiVPO<sub>4</sub>F oxidized under air can be probably defined as Li<sub>1-x</sub>VPO<sub>4</sub>F<sub>1-y</sub>O<sub>z</sub> (0 < x < 0.2, 0.9 < y ≤ 1, 0.9 < z ≤ 1) according to the comprehensive analytical results from TG–DTA, TG–DSC–MS, ICP–AES, SEM–EDS, XRF and XPS. This oxidation behavior is similar to the structural transformation from LiVPO<sub>4</sub>O to Li<sub>3</sub>V<sub>2</sub>(PO<sub>4</sub>)<sub>3</sub> in a mixed gas flow of H<sub>2</sub>/Ar [40]. When x = 0.1, y = 0.95 and z = 0.95, the defined Li<sub>1-x</sub>VPO<sub>4</sub>F<sub>1-y</sub>O<sub>z</sub> compound can be described Li<sub>0.9</sub>V–PO<sub>4</sub>F<sub>0.05</sub>O<sub>0.95</sub> and its structural parameters are displayed in Table S4 (Supplementary materials).

Compared these data with those in reported literature, it is obvious that the XRD pattern of Li<sub>1-x</sub>VPO<sub>4</sub>F<sub>1-y</sub>O<sub>z</sub> is different with that of LiVPO<sub>4</sub>F, VPO<sub>4</sub>F or their mixture but similar to the structure of LiVPO<sub>4</sub>O. Therefore, the obtained Li<sub>1-x</sub>VPO<sub>4</sub>F<sub>1-y</sub>O<sub>z</sub> may be a quasi new compound. Due to the replacement of fluorine by oxygen and partial volatilization loss of lithium, the electrochemical performances of sintered samples become poorer with the increase of sintering temperature. Besides, the valence change of vanadium induced by the partial replacement of fluorine with oxygen and partial volatilization loss of lithium also results in the color changes of samples from black to gray-green with the increase of sintering temperatures. Besides, endothermic peaks cannot be observed in the DTA curve as shown in Fig. 1. When the original LiVPO<sub>4</sub>F was heat-treated between 500 and 700 °C, it is found that there is no obvious weight loss and thermal behaviors in TG–DTA curves. When the sintering temperature was raised to 750 °C or higher one, it is found that the resulted powders disappeared completely after





**Fig. 5.** SEM images of  $\text{LiVPO}_4\text{F}$ -based samples heat-treated at different temperatures (a) The original; (b) 350 °C; (c) 550 °C; (d) 600 °C; (e) 650 °C; (f) 700 °C.

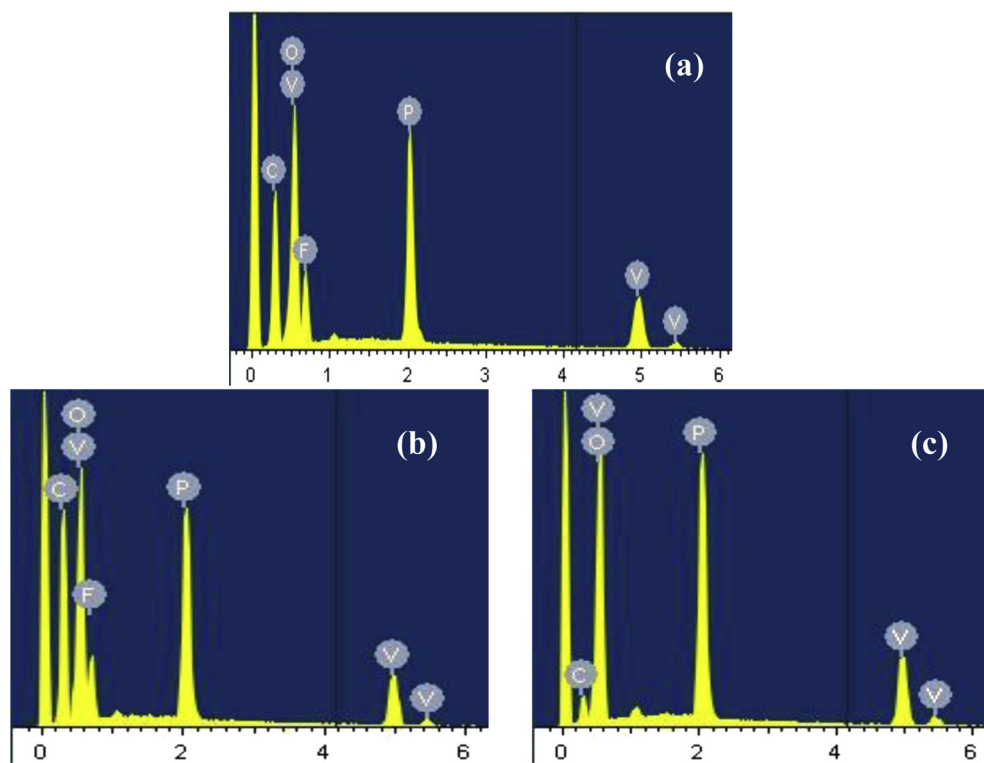


**Fig. 6.** EDS of the  $\text{LiVPO}_4\text{F}$ -based materials. (a) The original; (b) 350 °C; (c) 550 °C.

heat-treatment. At the same time, the inner wall of alumina crucible becomes black after heat-treatment. It is probably attributed to the diffusion of  $\text{LiVPO}_4\text{F}$ -based samples into the inner wall of alumina crucible after high temperature calcination. As a result, the whole oxidation process of  $\text{LiVPO}_4\text{F}$  under air can be probably described by the following equation:

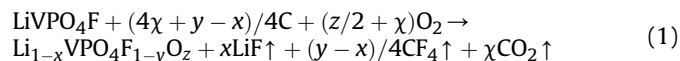


Fig. 8 shows the FTIR spectra of the  $\text{LiVPO}_4\text{F}$ -based samples prepared at different temperatures. When the sintering temperature was raised to  $550^\circ\text{C}$ , the resulting powder is more sensitive to air and water than the original sample and the sample obtained at  $350^\circ\text{C}$ . It absorbs more water and gas molecules under air, which is confirmed by the stronger stretching vibrations of O–H band at  $3430\text{ cm}^{-1}$  and the stronger bending vibrations of O–H bands at around  $1635\text{ cm}^{-1}$  as shown in Fig. 8a [41]. When  $\text{LiVPO}_4\text{F}$  was sintered at  $350$  and  $550^\circ\text{C}$  under air, the FTIR spectra of the oxidized powders have some obvious changes as shown in Fig. 8b.

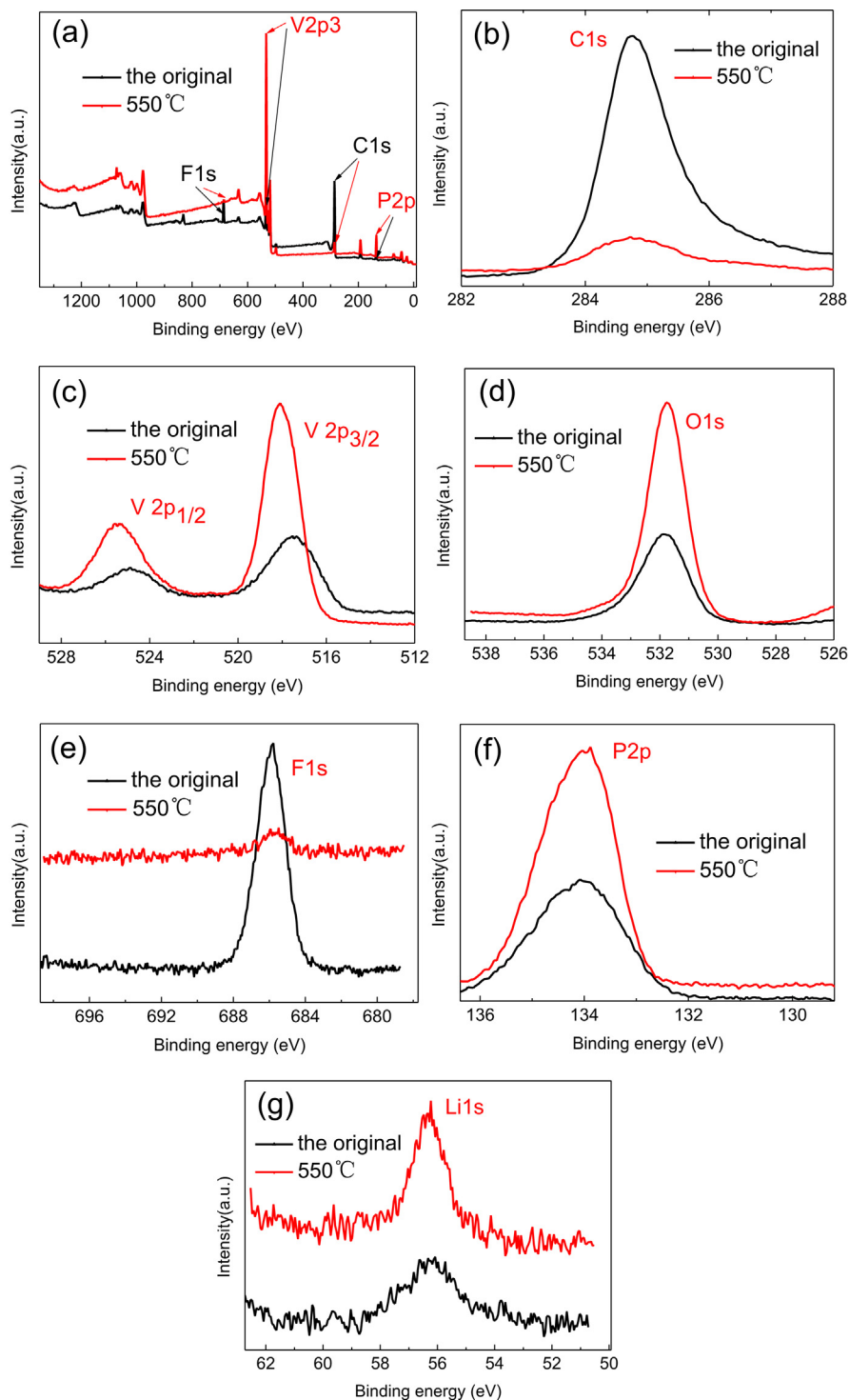


Fig. 7. Core level XPS spectra of the original and the sample sintered at  $550^\circ\text{C}$  for 30 min under air. (a) Survey; (b) C 1s; (c) V 2p; (d) O 1s; (e) F 1s; (f) P 2p; (g) Li 1s.

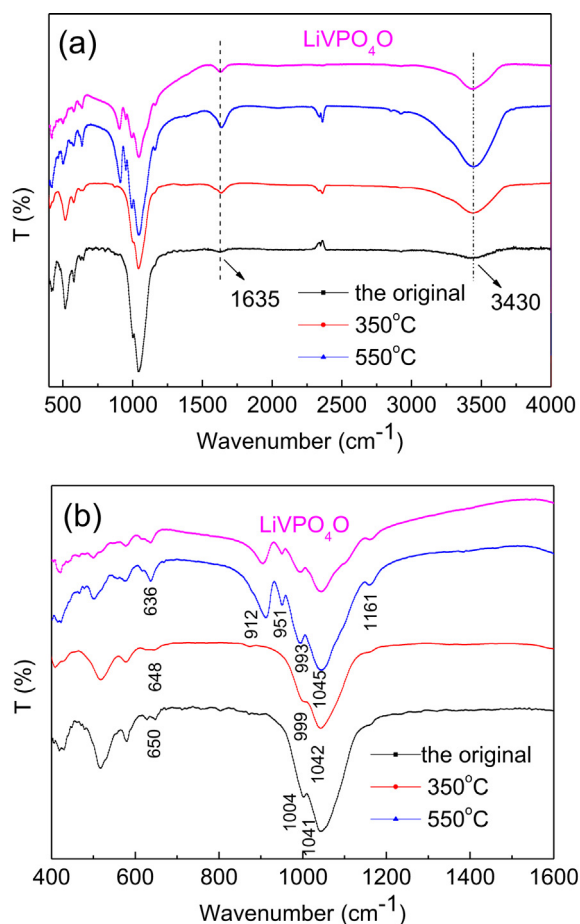


Fig. 8. The FTIR spectra of the  $\text{LiVPO}_4\text{F}$ -based samples heat-treated at different temperatures. (a) 400–4000  $\text{cm}^{-1}$ ; (b) 400–1600  $\text{cm}^{-1}$ .

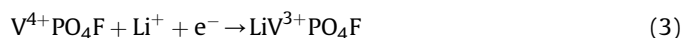
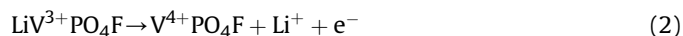
For instance, the stretching vibration frequencies of  $\text{V}=\text{O}$  band (1041, 1042 and 1045  $\text{cm}^{-1}$ ) have some blue-shifts, but the bending vibration frequencies of  $\text{O}-\text{V}-\text{O}$  band (650, 648 and 636  $\text{cm}^{-1}$ ) and the stretching vibration frequencies of  $\text{PO}_4$  tetrahedra (1004, 999 and 993  $\text{cm}^{-1}$ ) have some red-shifts. All these results are resulted from the partial volatilization loss of lithium and the replacement of fluorine by oxygen in the structure of  $\text{LiVPO}_4\text{F}$  after sintering under air. Besides, the powders sintered at 550  $^{\circ}\text{C}$  for 30 min under air have some new absorption peaks at 912, 951 and 1161  $\text{cm}^{-1}$ , which cannot be attributed to the stretching or bending vibrations of  $\text{V}-\text{O}$  bond in  $\text{V}_2\text{O}_5$ . Although  $\text{Li}_{1-x}\text{VPO}_4\text{F}_{1-y}\text{O}_z$  shows similar FTIR and XRD patterns with those of  $\text{LiVPO}_4\text{F}$ , it may be a new substance with a new structure because of these slight differences. It implies that these new bands come from the featured vibrations of  $\text{Li}_{1-x}\text{VPO}_4\text{F}_{1-y}\text{O}_z$ . Based on the previous report [42], it is found that the two new absorption peaks at 912 and 1161  $\text{cm}^{-1}$  can be ascribed to  $\text{V}=\text{O}$  and  $\text{P}-\text{O}$  bonds of  $\text{LiVPO}_4\text{O}$ , respectively. The infrared characteristic peak at 951  $\text{cm}^{-1}$  is contributed to the symmetric stretching vibration of the  $\text{PO}_4$  tetrahedra in the structure of  $\text{LiVPO}_4\text{O}$ . Therefore, the oxidized compound  $\text{Li}_{1-x}\text{VPO}_4\text{F}_{1-y}\text{O}_z$  is probable isostructure with the known mineral ambygonite,  $\text{LiVPO}_4\text{O}$ . These results are also accordance with the above TG-DTA, TG-DSC-MS, ICP-AES, SEM-EDS, XRF and XPS analysis.

Fig. 9a and b present the charge/discharge curves and corresponding differential capacity profile of  $\text{LiVPO}_4\text{F}$ -based samples cycled between 3.0 and 4.7 V at a current density of 10  $\text{mA g}^{-1}$ . The original material  $\text{LiVPO}_4\text{F}$  shows two operating potential plateaus at 4.25 and 4.30 V during the charge process, corresponding to a

total charge capacity of 176  $\text{mAh g}^{-1}$ . Upon discharge, the original material  $\text{LiVPO}_4\text{F}$  could deliver a discharge capacity of 112  $\text{mAh g}^{-1}$ , which corresponds to an operating potential plateau at 4.18 V as shown in Fig. 9a. However, its initial cycling coulomb efficiency is only 63.6% and lower than the first cycle charge efficiency (reaching to approximate 84.0%) reported by Barker [43], which is possibly resulted from the electrolyte decomposition formation of solid electrolyte interphase at high operating potentials ( $>4.0$  V). Moreover, the low first coulombic efficiency is also contributed to the poor kinetic behaviors of as-prepared sample with large particle size. Besides, there are three weak oxidation peaks appeared at 3.61, 3.69, 4.09 V during charge process and two weak reduction peaks appeared at 3.65, 3.57 V during discharge process in the CV curves of  $\text{LiVPO}_4\text{F}$ , which are corresponding to the lithiation/delithiation behaviors of the existence of  $\text{Li}_3\text{V}_2(\text{PO}_4)_3$  impurity. When  $\text{LiVPO}_4\text{F}$  are sintered at 350  $^{\circ}\text{C}$  for 30 min under air, the reversible capacity and cycling efficiency show a slight decrease as shown in Fig. 9c and d. When the sintering temperature is raised to 550  $^{\circ}\text{C}$ , the Li-storage capacities of samples decrease dramatically, i.e. the charge and discharge capacities are 57.5 and 21.6  $\text{mAh g}^{-1}$ , respectively, during the initial cycle. During the second cycle, the charge and discharge capacities of  $\text{Li}_{1-x}\text{VPO}_4\text{F}_{1-y}\text{O}_z$  are merely 53 and 22.2  $\text{mAh g}^{-1}$ , respectively. Viewed from the charge/discharge curves in Fig. 9a and the CVs in Fig. 9e,  $\text{Li}_{1-x}\text{VPO}_4\text{F}_{1-y}\text{O}_z$  exhibits unusual electrochemical behaviors with two delithiated slopes at 4.07 and 4.27 V in the charge process and two lithiated slopes at 3.75 and 3.85 V in the discharge process, which are accordance with the redox peaks in CV curves as seen in Fig. 9e. Yang observed similar redox peaks in the CV curves of  $\text{LiVPO}_4\text{O}$  [44]. It is found that the oxidation and reduction peaks in their CV curves are located at 4.14 and 3.84 V, respectively. It suggests that  $\text{Li}_{1-x}\text{VPO}_4\text{F}_{1-y}\text{O}_z$  has a different structure with that of  $\text{LiVPO}_4\text{F}$  but has a similar structure to that of  $\text{LiVPO}_4\text{O}$ . The structural evolutions resulted from the replacement of fluorine by oxygen during sintering under air should be attributable to the decrease of reversible capacities. As reported [44,45],  $\text{LiVPO}_4\text{O}$  samples prepared by solid state reactions always show poor electrochemical properties. Here, the  $\text{Li}_{1-x}\text{VPO}_4\text{F}_{1-y}\text{O}_z$  samples obtained at high temperature calcination show similar poor electrochemical behaviors to that of  $\text{LiVPO}_4\text{O}$  bulks. In addition, we could find that the polarization phenomenon of  $\text{LiVPO}_4\text{F}$ -based powders becomes more and more severe with the increase of sintering temperatures as shown in Fig. 9a and e. It indicates that the oxidation products of  $\text{LiVPO}_4\text{F}$  are not suitable as advanced cathode materials for lithium-ion batteries.

It is well known that the structural stability of electrode materials during lithiation/delithiation process plays a key factor on the cycling stability of lithium-ion batteries. In this paper, we adopt an *in-situ* X-ray diffraction technique to explore the structural evolutions of  $\text{LiVPO}_4\text{F}$ -based samples during charge/discharge processes. Detailed information is presented as follows.

Figs. 10 and 11 show the initial charge/discharge curves and corresponding *in-situ* XRD patterns of the original  $\text{LiVPO}_4\text{F}$  sample cycled at 10  $\text{mA g}^{-1}$  in 3.0–4.7 V. Each XRD pattern was taken for 12 min in the experiment. Based on the reversibility of the  $\text{V}^{3+}/\text{V}^{4+}$  redox couple, the lithium extraction/insertion reaction for  $\text{LiVPO}_4\text{F}$  can be summarized as:



As shown in Fig. 10, it could be found that there are two extraction plateaus appeared at 4.26 and 4.30 V in the initial charge curve of  $\text{LiVPO}_4\text{F}$ , which is similar to the previous reports [36,46–48]. It is thought that two energetically nonequivalent reactions

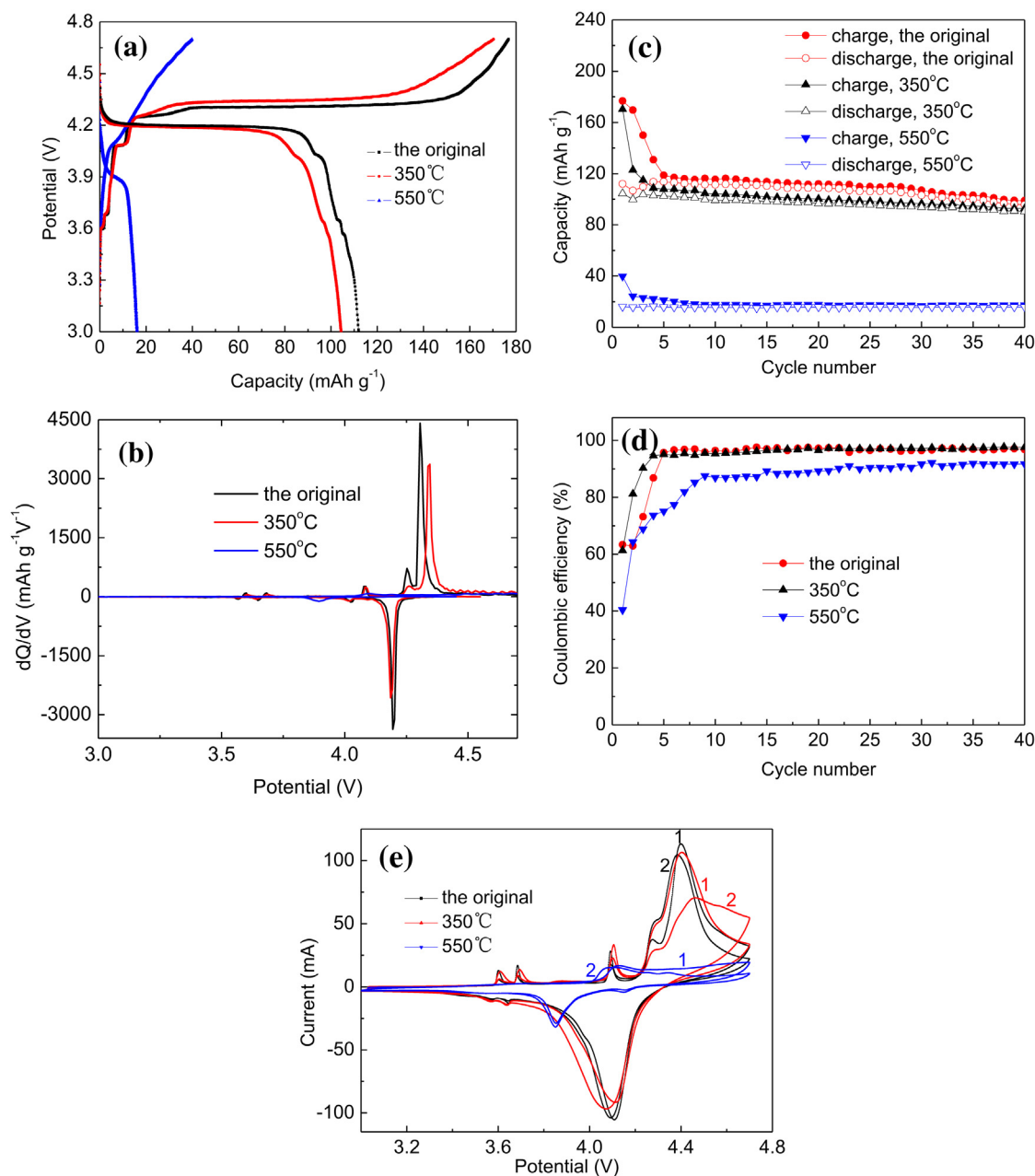


**Fig. 9.** (a) The initial galvanostatic charge/discharge curves of  $\text{LiVPO}_4\text{F}$ -based samples heat-treated at different temperatures; (b) Differential capacity profile; (c) Cycling performances; (d) Coulombic efficiencies; (e) Cyclic voltammograms.

corresponding to  $\text{Li}^+$  extraction from two noncrystallographically-equivalent Li sites in the structure of  $\text{LiVPO}_4\text{F}$  are the main reasons for the existence of the turning potential point between two extraction plateaus. However, only one site was found for  $\text{Li}^+$  in the structure model of  $\text{LiVPO}_4\text{F}$  as presented in the recent paper [49]. Based on the above discussions, it is considered that two Li sites in the structure of  $\text{LiVPO}_4\text{F}$  are different from each other. As a result, the molar formation Gibbs free energies of two delithiated products are different from each other. As well-known, the operating potential during charge/discharge process is determined by the difference of molar formation Gibbs free energies between reactant and product. Therefore, it is thought that the existence of two extraction plateaus in the initial charge curve of  $\text{LiVPO}_4\text{F}$  is contributed to the difference of molar formation Gibbs free energies of lithiated and delithiated products.

Viewed from the *in-situ* XRD data in Figs. 11 and 12, it is failed to observe the obvious shift of XRD peak positions during the initial delithiation process with  $x = 0.0\text{--}0.5$  in  $\text{Li}_{1-x}\text{VPO}_4\text{F}$ . However, the disappearance of the original  $\text{LiVPO}_4\text{F}$  and the appearance of an intermediate phase as 0.28 Li per formula extraction from the structure of  $\text{LiVPO}_4\text{F}$  should take place according to the phase transition point in the charge curve in Fig. 10 and the XRD patterns in Fig. 13, and the data in the charge process can be divided into two composition regions with  $x = 0.0\text{--}0.28$  and  $x = 0.28\text{--}1.0$  in  $\text{Li}_{1-x}\text{VPO}_4\text{F}$ . Based on the extracted lithium content as shown in Fig. 10, this intermediate compound is defined as  $\text{Li}_{0.72}\text{VPO}_4\text{F}$ , which is slightly different from  $\text{Li}_{0.70}\text{VPO}_4\text{F}$  as reported by Basir and  $\text{Li}_{0.67}\text{VPO}_4\text{F}$  as reported by Mba [46,49]. Based on the *in-situ* and *ex-situ* XRD patterns in Fig. 13, the intermediate phase  $\text{Li}_{0.72}\text{VPO}_4\text{F}$  is a new substance and its crystal structure is described in Table S2



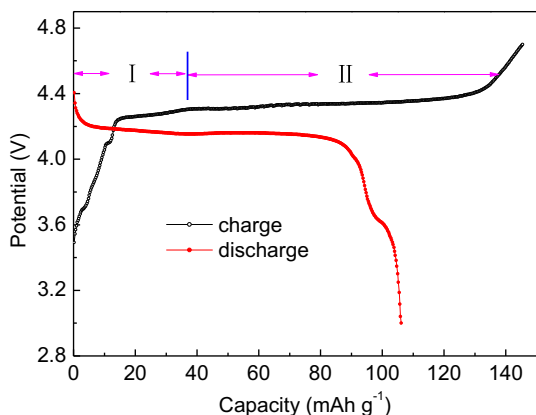


Fig. 10. The initial charge/discharge curves of  $\text{LiVPO}_4\text{F}$  cycled at  $10 \text{ mA g}^{-1}$  in 3.0–4.7 V.

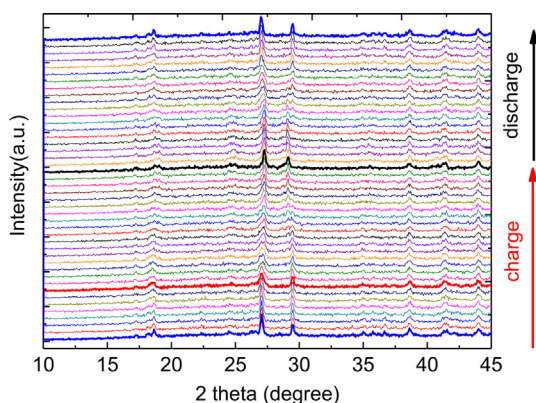


Fig. 11. In-situ XRD patterns of  $\text{LiVPO}_4\text{F}$  cycled at  $10 \text{ mA g}^{-1}$  in 3.0–4.7 V.

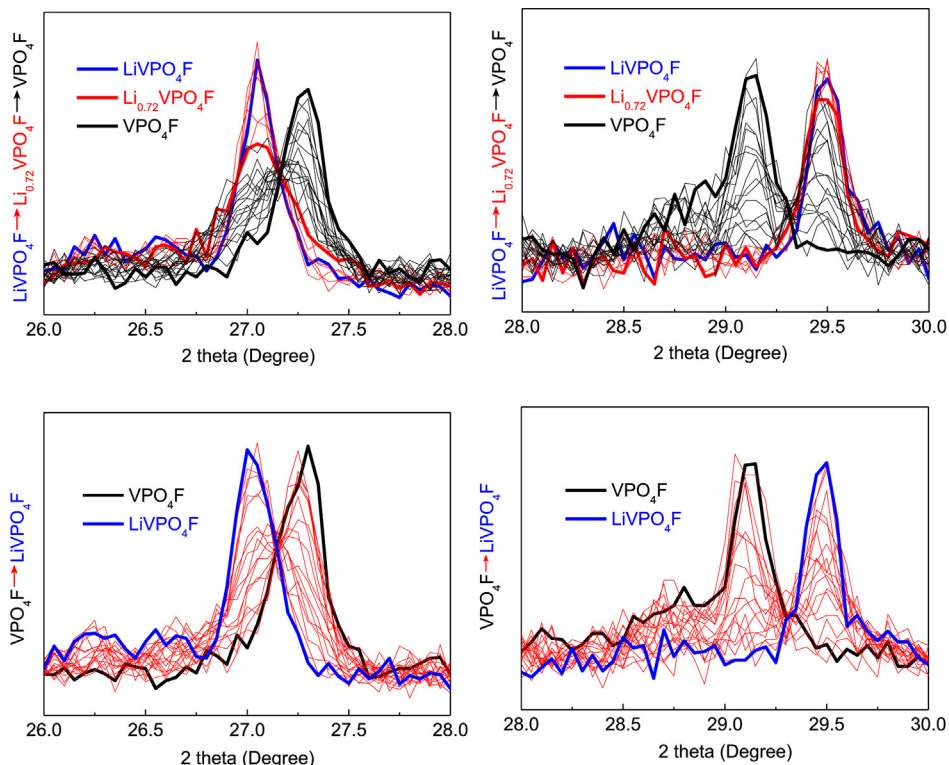


Fig. 12. Selected in-situ XRD patterns in the initial charge/discharge of  $\text{LiVPO}_4\text{F}$ .

(Supplementary materials). Here, all the *ex-situ* XRD patterns were collected by a cycling step-scan for 2 h per pattern, which is much longer than the *in-situ* XRD patterns for only 12 min per pattern. Along with further lithium ion extraction to the end of charge, the fractured diffraction peaks ( $2\theta = 27.10^\circ$  and  $29.50^\circ$ ) for  $\text{Li}_{0.72}\text{VPO}_4\text{F}$  disappear and the fractured diffraction peaks ( $2\theta = 27.26^\circ$  and  $29.10^\circ$ ) for  $\text{VPO}_4\text{F}$  appear. The detailed structural parameters of  $\text{VPO}_4\text{F}$  are described in Table S3 (Supplementary materials). As a result, the whole phase transition process during charge can be described as  $\text{LiVPO}_4\text{F} \rightarrow \text{Li}_{0.72}\text{VPO}_4\text{F} \rightarrow \text{VPO}_4\text{F}$ . It suggests that the charge processes of  $\text{LiVPO}_4\text{F}$  are two two-phase structural transitions.

Upon a discharge process to the end, the fractured diffraction peaks ( $2\theta = 27.26^\circ$  and  $29.2^\circ$ ) of  $\text{VPO}_4\text{F}$  disappear and the fractured diffraction peaks ( $2\theta = 27.1^\circ$  and  $29.5^\circ$ ) of  $\text{LiVPO}_4\text{F}$  reappear without the appearance of intermediate phase  $\text{Li}_{0.72}\text{VPO}_4\text{F}$  as the discharge curve and corresponding *in-situ* XRD patterns shown in Figs. 10–12. It implies that there is only one two-phase structural transition in the discharge process, i.e.  $\text{VPO}_4\text{F} \rightarrow \text{LiVPO}_4\text{F}$ . As a result, it can be concluded that the charge/discharge process of  $\text{LiVPO}_4\text{F}$  is an asymmetrical phase transformation as shown in Fig. 12. Moreover, it can be found that  $\text{LiVPO}_4\text{F}$  returns to its original phase through an asymmetrically full lithiation/delithiation process, which implies that the structure of  $\text{LiVPO}_4\text{F}$  could not be affected by repeated charge/discharge process. Therefore, the total lithium extraction/insertion reactions for  $\text{LiVPO}_4\text{F}$  can be described as:

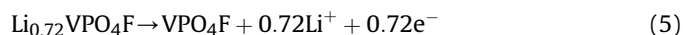
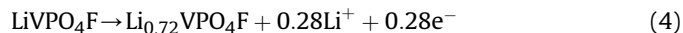


Fig. 14 shows the initial two charge/discharge curves of oxidized  $\text{LiVPO}_4\text{F}$  ( $550^\circ\text{C}$ ) cycled at  $5 \text{ mA g}^{-1}$  in 3.0–4.7 V. The decrease of

current density from  $10 \text{ mA g}^{-1}$  (Fig. 9a) to  $5 \text{ mA g}^{-1}$  (Fig. 14) results in the appearance of larger irreversible capacity from electrolyte oxidation decomposition at high potential regions. Based on the above analysis, it is known that  $\text{LiVPO}_4\text{F}$  sintered at  $550^\circ\text{C}$  for 30 min transforms to a new phase  $\text{Li}_{1-x}\text{VPO}_4\text{F}_{1-y}\text{O}_z$  ( $0 < x < 0.2$ ,  $0.9 < y \leq 1$ ,  $0.9 < z \leq 1$ ) with isostructure of  $\text{LiVPO}_4\text{FO}$ . Although  $\text{Li}_{1-x}\text{VPO}_4\text{F}_{1-y}\text{O}_z$  shows poor electrochemical performance, its structure is maintained as proven by the *in-situ* XRD patterns as shown in Figs. 15 and 16, S1 and S2 (Supplementary Materials). With a close observation, it is obvious that only a slight evolution of the intensity of diffraction peaks ( $2\theta = 27.25^\circ$  and  $29.75^\circ$ ) can be found without the shift of diffraction peaks upon the whole charge/discharge processes. The intensities of the diffraction peaks ( $2\theta = 27.25^\circ$  and  $29.75^\circ$ ) decrease slightly upon charge and become strong again during the discharge process. It tells that the structure of full delithiated compound is probably similar to that of the original  $\text{Li}_{1-x}\text{VPO}_4\text{F}_{1-y}\text{O}_z$  sample. By deducting the estimated capacity loss, the possible structure of delithiated  $\text{Li}_{1-x-m}\text{VPO}_4\text{F}_{1-y}\text{O}_z$  can be defined as  $\text{Li}_{0.65}\text{VPO}_4\text{FO}_{0.95}$  when  $x = 0.1$ ,  $y = 0.95$ ,  $z = 0.95$  and  $m = 0.25$  and its crystal structure can be described in

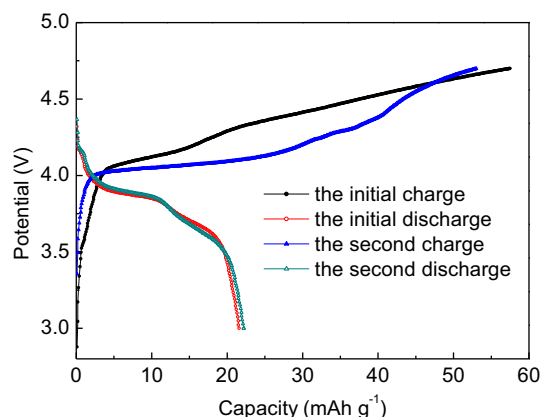


Fig. 14. The initial two charge/discharge curves of  $\text{LiVPO}_4\text{F}$  sintered at  $550^\circ\text{C}$  for 30 min cycled at  $5 \text{ mA g}^{-1}$  in 3.0–4.7 V.

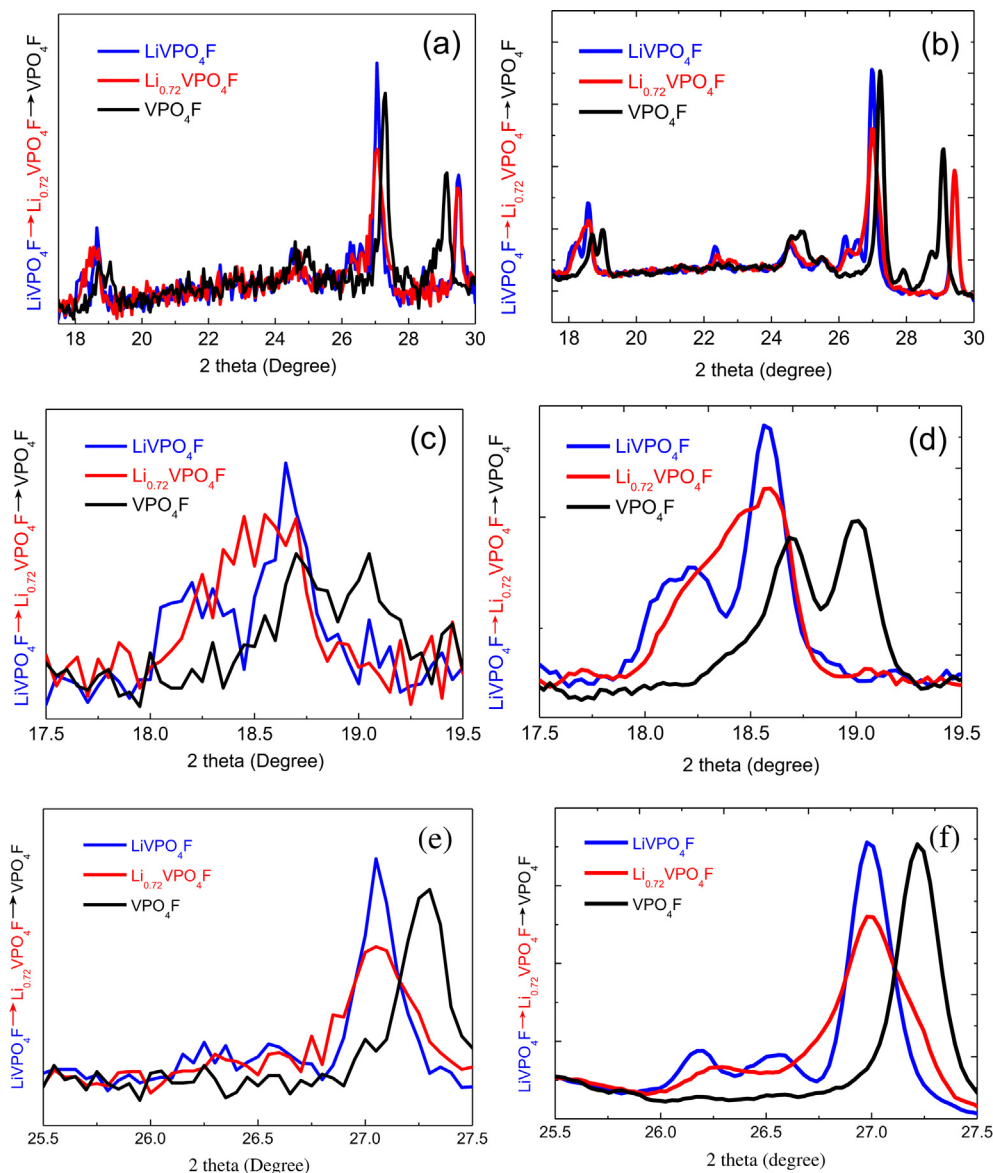


Fig. 13. A comparison of selected *in-situ* XRD patterns (a,c,e) and corresponding *ex-situ* XRD patterns (b,d,f) in the initial charge process of  $\text{LiVPO}_4\text{F}$ .

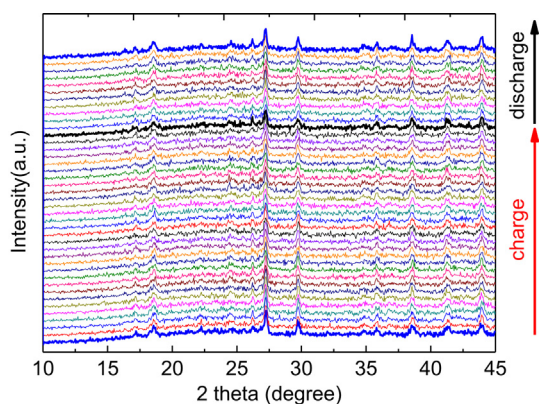
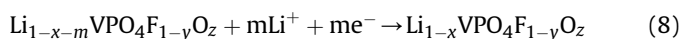


Fig. 15. *In-situ* XRD patterns of  $\text{LiVPO}_4\text{F}$  sintered at  $550\text{ }^\circ\text{C}$  for 30 min cycled at  $5\text{ mA g}^{-1}$  in 3.0–4.7 V during the first charge/discharge process.

Table S5 (Supplementary materials). Therefore, the total lithium extraction/insertion reactions for  $\text{Li}_{1-x}\text{VPO}_4\text{F}_{1-y}\text{O}_z$  can be probably described as:



Moreover, the remained XRD patterns during repeated cycles are also associated with the low lithium insertion/extraction contents. Therefore, it is considered that  $\text{Li}_{1-x}\text{VPO}_4\text{F}_{1-y}\text{O}_z$  ( $0 < x < 0.2$ ,  $0.9 < y \leq 1$ ,  $0.9 < z \leq 1$ ) is a stable but electrochemically inactive compound.

#### 4. Conclusions

By using powerful analytical techniques (TG–DTA, TG–DSC–MS, ICP–AES, SEM–EDS, XRF, XPS, FTIR, powder and *in-situ* XRD), this work identified the effects of oxidation on the structure and performance of  $\text{LiVPO}_4\text{F}$ , which has been considered as a promising cathode material for the next generation Li-ion batteries with an average high operating potential at 4.25 V and a reversible capacity of  $112\text{ mAh g}^{-1}$ . It exhibits one lithiated plateau at 4.18 V and two delithiated plateaus at 4.26 and 4.30 V, which is resulted from the formation of the intermediate phase  $\text{Li}_{0.72}\text{VPO}_4\text{F}$ . In this paper, a series of  $\text{LiVPO}_4\text{F}$ -based powders were prepared through sintering  $\text{LiVPO}_4\text{F}$  at different temperatures under air. When the original  $\text{LiVPO}_4\text{F}$  sample is sintered at  $350\text{ }^\circ\text{C}$ , its crystal structure shows no obvious change, but the X-ray diffraction peaks of oxidized sample obtained at  $550\text{ }^\circ\text{C}$  shift to higher Bragg positions. When the sintering temperature is raised to  $750\text{ }^\circ\text{C}$ , the resulting powders disappear completely. *In-situ* X-ray diffraction tests demonstrate that  $\text{LiVPO}_4\text{F}$  experiences an asymmetrical phase transformation upon a charge/discharge process, i.e.  $\text{LiVPO}_4\text{F} \rightarrow \text{Li}_{0.72}\text{VPO}_4\text{F} \rightarrow \text{VPO}_4\text{F}$  during lithium ion extraction and  $\text{VPO}_4\text{F} \rightarrow \text{LiVPO}_4\text{F}$  during lithium ion insertion without the appearance of the intermediate phase  $\text{Li}_{0.72}\text{VPO}_4\text{F}$ . In addition, When  $\text{LiVPO}_4\text{F}$  is sintered at  $550\text{ }^\circ\text{C}$ , an abrupt decrease in capacity is observed, and this compound exhibits unusual redox behaviors with two delithiated slopes at 4.07 and 4.27 V during the charge process and two lithiated slopes at 3.75 and 3.85 V during the discharge process. Furthermore, TG–DTA, TG–DSC–MS, ICP–AES, SEM–EDS, XRF, XPS, FTIR and powder XRD tests demonstrate the sample obtained at  $550\text{ }^\circ\text{C}$  can be defined as the formula of  $\text{Li}_{1-x}\text{VPO}_4\text{F}_{1-y}\text{O}_z$  ( $0 < x < 0.2$ ,  $0.9 < y \leq 1$ ,  $0.9 < z \leq 1$ ) with similar structure of  $\text{LiVPO}_4\text{O}$ . It is an unknown new substance with a stable structure as proven by *in-situ* X-ray

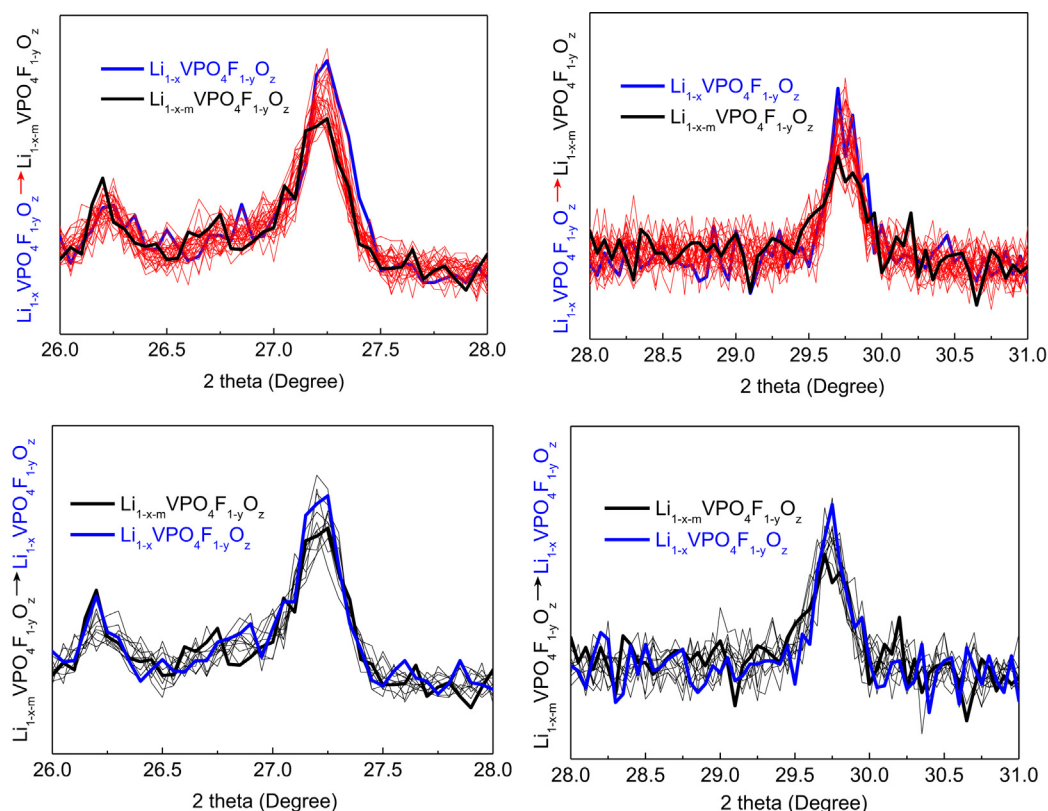


Fig. 16. Selected *in-situ* XRD patterns during the first charge/discharge process of  $\text{LiVPO}_4\text{F}$  sintered at  $550\text{ }^\circ\text{C}$  for 30 min cycled at  $5\text{ mA g}^{-1}$  in 3.0–4.7 V.



diffraction. Detailed structure information of  $\text{Li}_{1-x}\text{VPO}_4\text{F}_{1-y}$  needs to be further studied by neutron diffraction or synchrotron radiation techniques in the future work. Finally, the next step in our group is to explore the structural evolutions of  $\text{LiVPO}_4\text{F}$  and  $\text{Li}_{1-x}\text{VPO}_4\text{F}_{1-y}\text{O}_z$  ( $0 < x < 0.2$ ,  $0.9 < y \leq 1$ ,  $0.9 < z \leq 1$ ) in broad electrochemical windows (0.0–4.7 V).

## Acknowledgments

This work is sponsored by National 863 Program (2013AA050901) and National Natural Science Foundation of China (No. 51104092). The work is also supported by Graduate Student Research and Innovation Program of Ningbo University (2012) and K. C. Wong Magna Fund in Ningbo University, Open Foundation of State Key Laboratory of Materials Processing and Die & Mould Technology (2012-P01), Open Foundation of State Key Laboratory of Electronic Thin Films and Integrated Devices (KFJJ201209) and Opening Project of State Key Laboratory of High Performance Ceramics and Superfine Microstructure (SKL201308SIC).

## Appendix A. Supplementary data

Supplementary data related to this article can be found at <http://dx.doi.org/10.1016/j.jpowsour.2013.10.029>.

## References

- [1] B. Scrosati, *Nature* 373 (1995) 557–558.
- [2] M. Armand, J.M. Tarascon, *Nature* 451 (2008) 652–657.
- [3] J.M. Tarascon, M. Armand, *Nature* 414 (2001) 359–367.
- [4] B. Scrosati, J.J. Garche, *J. Power Sources* 195 (2010) 2419–2430.
- [5] Z.X. Wang, L.Q. Chen, X.J. Huang, *Prog. Chem.* 23 (2011) 284–301.
- [6] J.T. Li, J.C. Fang, H. Su, S.G. Sun, *Prog. Chem.* 23 (2011) 349–356.
- [7] P.G. Bruce, A.R. Armstrong, R.L. Gitzendanner, *J. Mater. Chem.* 9 (1999) 193–198.
- [8] T. Nodoseykin, S.S. Kim, Y. Nitta, *Electrochim. Acta* 52 (2006) 1467–1471.
- [9] F.K. Shokoohi, J.M. Tarascon, B.J. Wilkens, *Appl. Phys. Lett.* 59 (1991) 1260–1262.
- [10] H. Huang, C.H. Chen, R.C. Perego, E.M. Kelder, L. Chen, J. Schoonman, W.J. Weydanz, D.W. Nielsen, *Solid State Ionics* 127 (2000) 31–42.
- [11] A.K. Padhi, K.S. Nanjundaswamy, J.B. Goodenough, *J. Electrochem. Soc.* 144 (1997) 1188–1194.
- [12] B. Kang, G. Ceder, *Nature* 458 (2009) 190–193.
- [13] C. Chen, A.B. Yuan, H.B. Zhao, J.Q. Xu, *Ionics* 18 (2012) 635–641.
- [14] A. Yamada, S.C. Chung, K. Hinokuma, *J. Electrochem. Soc.* 148 (2001) A224–A229.
- [15] B.L. Ellis, K. Town, L.F. Nazar, *Electrochim. Acta* 84 (2012) 145–154.
- [16] G.Q. Liu, C.L. Zeng, K. Yang, *Electrochim. Acta* 47 (2002) 3239–3243.
- [17] A. Pan, J. Liu, J.G. Zhang, G.Z. Cao, W. Xu, Z.M. Nie, X. Jie, D. Choi, B.W. Arey, C.M. Wang, S.Q. Liang, *J. Mater. Chem.* 21 (2011) 1153–1161.
- [18] S.Q. Wang, Z.D. Lu, C.G. Li, C.H. Chen, Y.D. Yin, *J. Mater. Chem.* 21 (2011) 6365–6369.
- [19] S. Patoux, C. Wurm, M. Morcrette, G. Rousse, C. Masquelier, J. Power Sources 119–121 (2003) 278–284.
- [20] M.Y. Saidi, J. Barker, H. Huang, J.L. Swoyer, G. Adamson, *J. Power Sources* 119–121 (2003) 266–272.
- [21] T.N. Ramesh, K.T. Lee, B.L. Ellis, L.F. Nazar, *Electrochim. Solid State Lett.* 13 (2010) A43–A47.
- [22] I.K. Lee, S.W. Hyun, T. Kouh, I.B. Shim, C.S. Kim, *J. Appl. Phys.* 111 (2012) 07E38.
- [23] R. Tripathi, G. Popov, B.L. Ellis, A. Huq, L.F. Nazar, *Energy Environ. Sci.* 5 (2012) 6238–6246.
- [24] B. Xu, D.N. Qian, Z.Y. Wang, Y.S. Meng, *Mater. Sci. Eng. R.* 73 (2012) 51–65.
- [25] R.K.B. Gover, P. Burns, A. Bryan, M.Y. Saidi, J.L. Swoyer, J. Barker, *Solid State Ionics* 177 (2006) 2635–2638.
- [26] J. Barker, M.Y. Saidi, J.L. Swoyer, *J. Electrochem. Soc.* 150 (2003) A1394–A1398.
- [27] S. Hamelet, P. Gibot, M.C. Cabanas, D. Bonnin, C.P. Grey, J. Cabana, J.B. Leriche, J.R. Carvajal, M. Courty, S. Levasseur, P. Carlach, M.V. Thournout, J.M. Tarascon, C. Masquelier, *J. Mater. Chem.* 19 (2009) 3979–3991.
- [28] R. Ma, J. Shu, L. Hou, M. Shui, L.Y. Shao, D.J. Wang, Y.L. Ren, *Ionics* 19 (2012) 725–730.
- [29] J. Shu, M. Shui, D. Xu, Y.L. Ren, D.J. Wang, Q.C. Wang, R. Ma, W.D. Zheng, S. Gao, L. Hou, J.J. Xu, J. Cui, Z.H. Zhu, M. Li, *J. Mater. Chem.* 22 (2012) 3035–3043.
- [30] J. Shu, M. Shui, D. Xu, S. Gao, T.F. Yi, D.J. Wang, X. Li, Y.L. Ren, *Ionics* 17 (2011) 503–509.
- [31] N. Lyczko, A. Nzihou, P. Sharrock, A. Germeau, C. Toussaint, *Ind. Eng. Chem. Res.* 51 (2012) 292–300.
- [32] J. Barker, R.K.B. Gover, P. Burns, A. Bryan, M.Y. Saidi, J.L. Swoyer, *J. Power Sources* 146 (2005) 516–520.
- [33] T.F. Yi, Y. Xie, J. Shu, Z.H. Wang, C.B. Yue, R.S. Zhu, H.B. Qiao, *J. Electrochem. Soc.* 158 (2011) A266–A274.
- [34] A.R. Naghash, J.Y. Lee, *Electrochim. Acta* 46 (2001) 941–951.
- [35] Y.Y. Xia, T. Sakaia, T. Fujieda, X.Q. Yang, X. Sun, Z.F. Ma, J. McBreen, M. Yoshio, *J. Electrochem. Soc.* 148 (2001) A723–A729.
- [36] M.V. Reddy, G.V. Subba Rao, B.V.R. Chowdari, *J. Power Sources* 195 (2010) 5768–5774.
- [37] Y. Li, Z. Zhou, X.P. Gao, J. Yan, *J. Power Sources* 160 (2006) 633–637.
- [38] J.C. Zheng, B. Zhang, Z.H. Yang, *J. Power Sources* 202 (2012) 380–383.
- [39] Y.H. Rho, L.F. Nazar, L. Perry, D. Ryan, *J. Electrochem. Soc.* 154 (2007) A283–A289.
- [40] H.T. Kuo, N.C. Bagkar, R.S. Liu, C.H. Shen, D.S. Shy, X.K. Xing, J.F. Lee, J.M. Chen, *J. Phys. Chem. B* 112 (2008) 11250–11257.
- [41] X. Dai, H.H. Tang, P. Yang, C.F. Zhang, *Mater. Rev.* 19 (2005) 69–72.
- [42] K.L. Harrison, A. Manthiram, *Inorg. Chem.* 50 (2011) 3613–3620.
- [43] J. Barker, M.Y. Saidi, J.L. Swoyer, *J. Electrochem. Soc.* 151 (2004) A1670–A1677.
- [44] Y. Yang, H. Fang, J. Zheng, L. Li, G. Li, G. Yan, *Solid State Sci.* 10 (2008) 1292–1298.
- [45] B.M. Azmi, T. Ishihara, H. Nishiguchi, Y. Takita, *J. Power Sources* 146 (2005) 525–528.
- [46] N.I. Basir, J. Barker, C. Masquelier, C. in: *LiBD-4 Meeting*, Arcachon, France, September 20–25, 2009.
- [47] J.M.A. Mba, L. Croguennec, N.I. Basir, J. Barker, C. Masquelier, *J. Electrochem. Soc.* 159 (2012) A1171–A1175.
- [48] J. Barker, R.K.B. Gover, P. Burns, A. Bryan, M.Y. Saidi, J.L. Swoyer, *J. Electrochem. Soc.* 152 (2005) A1776–A1779.
- [49] J.M.A. Mba, C. Masquelier, E. Suard, L. Croguennec, *Chem. Mater.* 24 (2012) 1223–1234.